

SENSITIVITY OF AN IMAGING SPACE INFRARED INTERFEROMETER

Tadashi Nakajima

National Astronomical Observatory, 2-21-1 Osawa, Mitaka, 181-8588,
Japan

tadashi.nakajima@nao.ac.jp

and

Hideo Matsuhara

The Institute of Space and Astronautical Science, 3-1-1 Yoshinodai,
Sagamihara, 229-8510, Japan

maruma@ir.isas.ac.jp

We study the sensitivities of space infrared interferometers. We formulate the signal-to-noise ratios of infrared images obtained by aperture synthesis in the presence of source shot noise, background shot noise and detector read noise. We consider the case in which n beams are pairwise combined at $n(n - 1)/2$ detectors, and the case in which all the n beams are combined at a single detector. We apply the results to future missions, Terrestrial Planet Finder and Darwin. We also discuss the potential of a far-infrared interferometer for a deep galaxy survey. © 2018 Optical Society of America

Accepted for publication in Applied Optics

OCIS codes: 110.3080, 110.4280, 120.3180

1. Introduction

Early in the 21st century space infrared observatories such as ASTRO-F,¹ Space Infrared Telescope Facility (SIRTF),² Far Infrared and Submillimeter Telescope (FIRST),³ and Space Infrared Telescope for Cosmology and Astrophysics (SPICA)⁴ are planned to study the formation of planets, stars, and galaxies. The improvement in sensitivity is so great that the source detection limits of these space observatories are expected to be set by source confusion, especially in the far infrared. To further improve the source detection limits, individual sources need to be resolved by an infrared interferometer. Therefore it is important to quantify the sensitivity of a space infrared interferometer for the purpose of synthesis imaging.

Following the observatories, space infrared interferometers such as the Terrestrial Planet Finder (TPF)⁵ and Darwin⁶ are considered, with an emphasis on the detection of terrestrial planets around nearby stars. TPF and Darwin will consist of several radiation cooled apertures and will be capable of synthesis imaging as well as planet detection by nulling interferometry. The detection limits of these interferometers for general synthesis imaging are of great interest. Among many applications of synthesis imaging with a space infrared interferometer, we are particularly interested in deep galaxy count by which the history of galaxy formation can be studied. We discuss how a TPF-like interferometer operated in the far infrared can improve the number count data of high redshift galaxies.

The beam combination geometry is a major issue in studying the sensitivity of an interferometer. One extreme is the nC_2 interferometer, in which n beams are divided into $n(n-1)$ subbeams and they are pairwise combined at ${}^nC_2 = n(n-1)/2$ detectors. There is one detector for each baseline. The other extreme is the nC_n interferometer in which all the n beams are combined at ${}^nC_n = 1$ detector. Prasad and Kulkarni⁷ (henceforth PK89) have rigorously analyzed the SNRs of the nC_2 and nC_n interferometers for spectrally narrow light in the presence of source shot noise and concluded that the sensitivities of both interferometers are essentially the same apart from a numerical factor. The results by PK89 are applicable to optical interferometry, but not to infrared interferometry because of the presence of thermal background and detector read noise. The beam combination geometry can have an impact on the sensitivity in the infrared for instance because of the number of detector pixels which affects the total read noise. The beam combination geometry may also have a major impact on the architecture of the space interferometer.

Baseline redundancy is a factor that affects the SNR of a synthesis image for a given number of apertures. Since the number of apertures deployed or flown separately in space is likely to be limited, it is important to gain uv coverage by using nonredundant baselines. Throughout this paper, we only consider interferometers with nonredundant baselines.

There are two types of noise which appear in aperture synthesis, one of which is removable while the other is intrinsic and not removable. Sampling noise is potentially introduced by the incompleteness of uv coverage. However, deconvolution techniques such as CLEAN and Maximum Entropy Method (MEM),⁸ when applied to radio interferometric data, appear to compensate for sampling noise. We thus regard sampling noise as removable noise. On the other hand, noise resulting from the photodetection process is not removable. The SNR of a dirty image to which deconvolution has not been applied is limited by photodetection noise. Here we derive the SNR of a dirty image as determined by source shot noise, thermal background shot noise, and detector read noise, and equate it to the SNR of the synthesized image.

There are two different methods by which a synthesized image can be constructed from the visibility data: inversion without total counts and true inversion. In the former, the zero frequency phasor is neglected, implying that the total number of photons in the synthesized image is zero. Despite this seemingly unattractive feature, this is the standard method in radio astronomy. In the latter method, the van Cittert-Zernike theorem is strictly applied and the zero frequency phasor as well as the $n(n - 1)/2$ complex phasors is used. The image produced by this technique has the desirable property of nonnegativity. In the presence of additive thermal background which overwhelms the signal, the magnitude of the zero frequency phasor is much greater than those of other phasors. The zero frequency phasor determines the DC offset level due to thermal background in the synthesized image. Not only is this background of little astronomical interest, it is also a major source of Poisson fluctuations. Therefore in this paper we prefer the former method and consider only the inversion without total counts as in radio astronomy.

We analyze the SNRs of space interferometers in three steps. First, we formulate the SNRs of nC_2 and nC_n interferometers in the presence of source shot noise, thermal background shot noise and detector read noise in §2 and §3 respectively. These formulae cover optical and infrared interferometers. Second, we consider spectrally broad light for which fringe dispersion becomes an issue. Fringes of the nC_2 interferom-

eter can always be dispersed while those of the nC_n interferometer can be dispersed only in the case of a one dimensional baseline configuration. We discuss the tradeoff between the nC_2 and nC_n interferometers including the dimensionality of the baseline configuration in §4. Third, we apply the results of our analysis to planned interferometers. We present the sensitivities of a TPF-like interferometer and a Darwin-like one in §5. Finally in §6 we discuss the capability of the TPF-like interferometer from the point of view of deep galaxy count.

2. nC_2 Interferometer

A. Fringe Phasor Estimator

Let there be n identical principal apertures from which we derive n main beams. Each beam is divided into $n - 1$ subbeams by the use of beam splitters. The resulting $n(n - 1)$ subbeams are combined pairwise on $n_b = n(n - 1)/2$ detectors where n_b is also the number of baselines.

The fringe pattern is formed at the focal plane of each detector. For spectrally narrow light, a one-dimensional detector is sufficient (Fig. 1). For spectrally broad light, the fringes can be dispersed in the cross fringe direction, in which case a two-dimensional detector is used. For a focal plane interferometer of this type, the influence of source shot noise on fringe phasor estimation has been fully formulated^{9, 10}. Let the interferometer be illuminated by a source upon a spatially smooth background. The intensity pattern on the r^{th} detector (r^{th} baseline) is given by

$$\langle I_r(\mathbf{x}) \rangle = 2 \langle I_0 \rangle \left[1 + \gamma_r \cos(\kappa \mathbf{x} \cdot \mathbf{B}_r / d + \phi_r) \right], \quad (1)$$

where $\langle I_0 \rangle$ is the average intensity in each subbeam at the detector, \mathbf{B}_r is the baseline vector, $\kappa = 2\pi/\lambda$ is the wave number, and d is the distance between the aperture plane and the detector, \mathbf{x} is the spatial vector in the detector plane, and $\gamma_r \exp(i\phi_r)$ is the complex visibility function at the baseline vector \mathbf{B}_r . In deriving (1), we have assumed that the incident light is spectrally narrow so that the fringe visibility depends only on the spatial correlation of the field.

Because of the presence of background illumination,

$$I_0 = I_0^s + I_0^b, \quad (2)$$

where I_0^s and I_0^b are source and background intensities respectively. Let γ_r^s be the fringe visibility of the source in the absence of the background, then

$$\gamma_r = \frac{I_0^s}{I_0^s + I_0^b} \gamma_r^s. \quad (3)$$

The complex visibility function $\gamma_r^s \exp(i\phi_r)$ is determined by the uv coordinates of the r^{th} baseline (u, v) and the source brightness distribution on the sky $S(x, y)$ by a Fourier transform relation:

$$\gamma_r^s \exp(i\phi_r) = \frac{\int S(x, y) \exp\{-2\pi i(ux + vy)\} dx dy}{\int S(x, y) dx dy}. \quad (4)$$

In an effort to reduce the clutter in the equations we henceforth drop the vector notation, but bear in mind that spatial frequencies, pixel locations, etc. are really vectors. The photoelectron detection theory⁹ takes into account the discrete nature of both photons and detector pixels. The average photoelectron count $\langle k_r(p) \rangle$ at the pixel location specified by the integer index p of the detector is proportional to $\langle I(x) \rangle$:

$$\langle k_r(p) \rangle = 2 \langle K_0 \rangle \left[1 + \gamma_r \cos(p\omega_r + \phi_r) \right]. \quad (5)$$

Here, $\langle \dots \rangle$ denotes averaging over the photoelectron-detection process. K_0 is the discrete version of I_0 . The product $p\omega_r$ is understood to be the scalar product of the pixel position vector \mathbf{p} and the spatial frequency ω_r expressed in inverse pixel units.

Let $\langle C \rangle$ be the average number of photoelectrons detected by the entire interferometer in one integration period, and let $2\langle N \rangle$ be the average number of photoelectrons per detector of each baseline per integration time. Clearly then, $\langle C \rangle = 2\langle N \rangle n_b$, and thus $\langle N \rangle = \langle C \rangle / \{n(n-1)\}$. According to (5), the average number of photoelectrons per detector is equal to $2\langle K_0 \rangle P$, and thus $\langle K_0 \rangle P = \langle N \rangle$, where P is the number of detector pixels.

Due to read noise $r_r(p)$, each measurement of the pixel p yields $l_r(p)$ given by

$$l_r(p) = k_r(p) + r_r(p), \quad (6)$$

where $r_r(p)$ is a Gaussian random number with zero mean and a standard deviation σ .

The fringe phasor for the baseline r is operationally defined as

$$y_r = \sum_{p=1}^P l_r(p) \exp(-ip\omega_r). \quad (7)$$

Walkup and Goodman have shown that the quantity

$$z_r = \sum_{p=1}^P k_r(p) \exp(-ip\omega_r) \quad (8)$$

is an optimum estimator of the actual fringe phasor under shot noise limited condition in the presence of constant background.⁹ Since

$$\langle \sum_{p=1}^P r_r(p) \exp(-ip\omega_r) \rangle = \sum_{p=1}^P \langle r_r(p) \rangle \exp(-ip\omega_r) = 0, \quad (9)$$

y_r is an optimum estimator of the fringe phasor in the presence of detector read noise.

The average of the phasor y_r over many coherent integration interval is given by

$$Y_r = \langle y_r \rangle = \langle N \rangle \gamma_r \exp(i\phi_r). \quad (10)$$

B. Inversion

The synthesized image is the real portion of the Fourier transform of the spatial coherence function:

$$\begin{aligned} i_1(q) &= \operatorname{Re} \left[\sum_{r=1}^{n_b} y_r \exp(+i\omega_r q) \right] \\ &= \sum_r [\operatorname{Re}(y_r) \cos(\omega_r q) - \operatorname{Im}(y_r) \sin(\omega_r q)]. \end{aligned} \quad (11)$$

Index q refers to pixels in the synthesized image; in particular q ranges from $-Q/2$ to $+Q/2$, and $q = 0$ refers to the central pixel in the synthesized image. The variable $i_1(q)$ refers to the image obtained from one set of visibility data. Note that the sense of Fourier transform used in (11) is consistent with the definition of y_r . The mean image $I_1(q)$ is the average of $i_1(q)$ and is given by

$$I_1(q) = \operatorname{Re} \left[\sum_{r=1}^{n_b} Y_r \exp(+i\omega_r q) \right], \quad (12)$$

which by virtue of (10), can be simplified to yield

$$\begin{aligned} I_1(q) &= \langle N \rangle \sum_r \gamma_r \cos(\omega_r q + \phi_r) \\ &= \langle N \rangle \sum_r \frac{I_0^s}{I_0^s + I_0^b} \gamma_r^s \cos(\omega_r q + \phi_r). \end{aligned} \quad (13)$$

The image $I_1(q)$ is referred to as the dirty image in the parlance of radio astronomy. The dirty image is the convolution of the true image and the Fourier transform of the spatial frequency sampling function or the dirty beam. A synthesized image can be obtained from the dirty image by deconvolution.

The variance $V[i_1(q)]$ in the synthesized image $i_1(q)$ is given by

$$\begin{aligned} V[i_1(q)] &= \langle i_1(q)^2 \rangle - \langle i_1(q) \rangle^2 \\ &= \sum_{r=1}^{n_b} \sum_{s=1}^{n_b} \left\{ \begin{aligned} &[\langle \operatorname{Re}(y_r) \operatorname{Re}(y_s) \rangle - \langle \operatorname{Re}(y_r) \rangle \langle \operatorname{Re}(y_s) \rangle] \cos(\omega_r q) \cos(\omega_s q) \\ & - [\langle \operatorname{Re}(y_r) \operatorname{Im}(y_s) \rangle - \langle \operatorname{Re}(y_r) \rangle \langle \operatorname{Im}(y_s) \rangle] \cos(\omega_r q) \sin(\omega_s q) \\ & - [\langle \operatorname{Im}(y_r) \operatorname{Re}(y_s) \rangle - \langle \operatorname{Im}(y_r) \rangle \langle \operatorname{Re}(y_s) \rangle] \sin(\omega_r q) \cos(\omega_s q) \\ & + [\langle \operatorname{Im}(y_r) \operatorname{Im}(y_s) \rangle - \langle \operatorname{Im}(y_r) \rangle \langle \operatorname{Im}(y_s) \rangle] \sin(\omega_r q) \sin(\omega_s q) \end{aligned} \right\}. \end{aligned} \quad (14)$$

The problem of estimating the variance of the image reduces to that of estimating three types of covariance term: $\operatorname{cov}[\operatorname{Re}(y_r), \operatorname{Re}(y_s)]$, $\operatorname{cov}[\operatorname{Re}(y_r), \operatorname{Im}(y_s)]$, and $\operatorname{cov}[\operatorname{Im}(y_r), \operatorname{Im}(y_s)]$.

$$\begin{aligned} \operatorname{cov}[\operatorname{Re}(y_r), \operatorname{Re}(y_s)] &= [\langle \operatorname{Re}(y_r) \operatorname{Re}(y_s) \rangle - \langle \operatorname{Re}(y_r) \rangle \langle \operatorname{Re}(y_s) \rangle] \\ &= \sum_{p=1}^P \sum_{p'=1}^P [\langle l_r(p) l_s(p') \rangle - \langle l_r(p) \rangle \langle l_s(p') \rangle] \cos(\omega_r p) \cos(\omega_s p'). \end{aligned} \quad (15)$$

where

$$\langle l_r(p) l_s(p') \rangle - \langle l_r(p) \rangle \langle l_s(p') \rangle = \langle k_r(p) k_s(p') \rangle - \langle k_r(p) \rangle \langle k_s(p') \rangle$$

$$\begin{aligned}
& + \langle k_r(p)r_s(p') \rangle - \langle k_r(p) \rangle \langle r_s(p') \rangle \\
& + \langle r_r(p)k_s(p') \rangle - \langle r_r(p) \rangle \langle k_s(p') \rangle \\
& + \langle r_r(p)r_s(p') \rangle - \langle r_r(p) \rangle \langle r_s(p') \rangle. \quad (16)
\end{aligned}$$

There is no correlation of shot noise between different detectors or between different pixels of the same detector. The correlation remains only for the same pixel. There is no correlation of shot noise and read noise even for the same detector pixel. And there is no correlation of read noise between different detectors or between different pixels of the same detector. The correlation exists only for the same pixel. Therefore

$$\langle k_r(p)k_s(p') \rangle - \langle k_r(p) \rangle \langle k_s(p') \rangle = \delta_{rs}\delta_{pp'} \langle k_r(p) \rangle, \quad (17)$$

$$\langle k_r(p)r_s(p') \rangle - \langle k_r(p) \rangle \langle r_s(p') \rangle = \langle r_r(p)k_s(p') \rangle - \langle r_r(p) \rangle \langle k_s(p') \rangle = 0, \quad (18)$$

and

$$\langle r_r(p)r_s(p') \rangle - \langle r_r(p) \rangle \langle r_s(p') \rangle = \delta_{rs}\delta_{pp'}\sigma^2. \quad (19)$$

Therefore

$$\langle l_r(p)l_s(p') \rangle - \langle l_r(p) \rangle \langle l_s(p') \rangle = \delta_{rs}\delta_{pp'}(\langle k_r(p) \rangle + \sigma^2), \quad (20)$$

and

$$\begin{aligned}
\text{cov}[Re(y_r), Re(y_s)] &= V[Re(y_r)]\delta_{rs} \\
&= \delta_{rs} \sum_p (\langle k_r(p) \rangle + \sigma^2) \cos(\omega_r p)^2 \\
&= \delta_{rs}(\langle N \rangle + \frac{P\sigma^2}{2}). \quad (21)
\end{aligned}$$

Similarly, one can show that

$$\text{cov}[Re(y_r), Im(y_s)] = \text{cov}[Im(y_r), Re(y_s)] = 0, \quad (22)$$

and

$$\text{cov}[Im(y_r), Im(y_s)] = \delta_{rs}(\langle N \rangle + \frac{P\sigma^2}{2}). \quad (23)$$

Substituting the nonzero covariance elements (21) and (23) into (14), we obtain

$$\begin{aligned} V[i_1(q)] &= \sum_r \left\{ \left(\langle N \rangle + \frac{P\sigma^2}{2} \right) \cos^2(\omega_r q) + \left(\langle N \rangle + \frac{P\sigma^2}{2} \right) \sin^2(\omega_r q) \right\} \\ &= \sum_r \left(\langle N \rangle + \frac{P\sigma^2}{2} \right) \\ &= n_b \left(\langle N \rangle + \frac{P\sigma^2}{2} \right) = \frac{\langle C \rangle}{2} + n_b \frac{P\sigma^2}{2}. \end{aligned} \quad (24)$$

In (24), the term $\langle C \rangle / 2$ is due to shot noise and the term $n_b P\sigma^2 / 2$ is due to read noise. Now we consider the specific case of a point source ($\gamma_r^s = 1$) at the phase center ($\phi_r = 0$) for which $I_1(0) = \frac{\langle C \rangle}{2}$. Since the source is located at the phase center, the SNR of the central pixel in the image is indicative of the SNR in the image:

$$\frac{I_1(0)}{\sqrt{V[i_1(0)]}} = \frac{(\langle C \rangle / 2) \{ I_0^s / (I_0^s + I_0^b) \}}{\sqrt{\langle C \rangle / 2 + n_b P\sigma^2 / 2}}. \quad (25)$$

3. nC_n Interferometer

In an nC_n interferometer, all n beams interfere on a single detector and n_b fringes are superposed. Both the baseline configuration and the detector can be either one dimensional or two dimensional. As an example, a two dimensional 3C_3 interferometer is schematically presented in Fig. 2. A special case is the combination of a one dimensional baseline configuration and a two dimensional detector for which the superposed fringes are dispersed in the cross fringe direction so that spectrally broad light can be used without bandwidth smearing. We call an nC_n interferometer of this type an ${}^nC'_n$ interferometer. A ${}^3C'_3$ interferometer is schematically shown in Fig. 3. Application of (7) with different spatial frequencies results in extraction of n_b fringe phasors and the image may be synthesized in the usual fashion.

A. Fringe phasor estimator

Let the interferometer be composed of n identical apertures and let it be illuminated by a source and a spatially smooth background. The classical intensity distribution of the interference pattern for the n apertures has the average value

$$\langle I(\mathbf{x}) \rangle = \langle I_0 \rangle \left[n + 2 \sum_{g < h} \gamma_{gh} \cos(\kappa \mathbf{x} \cdot \mathbf{B}_{gh}/d + \phi_{gh}) \right], \quad (26)$$

where the various symbols have meanings similar to those in (1). gh denotes the baseline gh corresponding to the apertures g and h . Let $\langle k(\mathbf{p}) \rangle$ denote the photoelectron count distribution due to $\langle I(\mathbf{x}) \rangle$. As in §2, we discontinue the vector notation, assume that the total number of pixels is P , and note that $\langle k(p) \rangle$ is proportional to $\langle I(x) \rangle$:

$$\langle k(p) \rangle = \langle Q_0 \rangle \left[n + \sum_{g < h} \gamma_{gh} \cos(p\omega_{gh} + \phi_{gh}) \right]. \quad (27)$$

Here $\langle Q_0 \rangle$ has approximately the same meaning as $\langle K_0 \rangle$ in §2. However, since there is no beam splitting, $\langle Q_0 \rangle = (n - 1) \langle K_0 \rangle$. Due to read noise $r(p)$, each measurement of the pixel p yields $l(p)$ counts:

$$l(p) = k(p) + r(p), \quad (28)$$

where $r(p)$ is a Gaussian random number with zero mean and a standard deviation σ .

In a typical setup, one can imagine integrating on a two dimensional detector for a period equal to the coherent integration interval. A Fourier transform of the resulting image yields $2n_b$ peaks, pairwise symmetrical about the origin, which can be identified with the n_b fringe phasors corresponding to the n_b spatial-frequency components. Let y_{gh} be the fringe phasor estimator corresponding to the baseline gh , then

$$y_{gh} = \sum_{p=1}^P l(p) \exp(-ip\omega_{gh}). \quad (29)$$

Here y_{gh} is an optimum estimator of the fringe phasor for the baseline gh . The mean phasor on the ij baseline is given by

$$\begin{aligned}
Y_{ij} &= \langle Q_0 \rangle \sum_p \exp(-ip\omega_{ij}) \left[n + 2 \sum_{g < h} \gamma_{gh} \cos(p\omega_{gh} + \phi_{gh}) \right] + \sum_p \langle r(p) \rangle \exp(-ip\omega_{ij}) \\
&= \langle Q_0 \rangle \sum_p \sum_{g < h} \gamma_{gh} \left\{ \exp(i\phi_{gh}) \exp[ip(\omega_{gh} - \omega_{ij})] \right. \\
&\quad \left. + \exp(-i\phi_{gh}) \exp[-ip(\omega_{gh} + \omega_{ij})] \right\}.
\end{aligned} \tag{30}$$

Since the baselines are nonredundant, $\omega_{ij} \neq \omega_{gh}$, unless (ij) and (gh) refer to the same baseline.

Therefore only the $g = i, h = j$ terms remains in (30):

$$Y_{ij} = Z_{ij} = \langle M \rangle \gamma_{ij} \exp(i\phi_{ij}), \tag{31}$$

where we define $\langle M \rangle = P \langle Q_0 \rangle = \langle C \rangle / n$.

B. Inversion

The dirty image, $i_2(q)$ is given by

$$\begin{aligned}
i_2(q) &= \operatorname{Re} \left[\sum_{i < j} y_{ij} \exp(iq\omega_{ij}) \right] \\
&= \sum_{i < j} \left[\operatorname{Re}(y_{ij}) \cos(q\omega_{ij}) - \operatorname{Im}(y_{ij}) \sin(q\omega_{ij}) \right].
\end{aligned} \tag{32}$$

Using (31), we find the mean synthesized image to be

$$\begin{aligned}
I_2(q) &= \operatorname{Re} \left[\sum_{i < j} Y_{ij} \exp(+iq\omega_{ij}) \right] \\
&= \langle M \rangle \sum_{i < j} \gamma_{ij} \cos(q\omega_{ij} + \phi_{ij}).
\end{aligned} \tag{33}$$

The derivation of the variance $V[i_2(q)]$ in the synthesized image $i_2(q)$ is somewhat lengthy and given in Appendix A. The result is:

$$\begin{aligned}
V[i_2(q)] &= \frac{n \langle M \rangle + P\sigma^2}{2} n_b + \langle M \rangle (n-2) \sum_{i < j} \gamma_{ij} \cos(q\omega_{ij} + \phi_{ij}) \\
&= \frac{n \langle M \rangle + P\sigma^2}{2} n_b + \langle M \rangle (n-2) \sum_{i < j} \frac{I_0^s}{I_0^s + I_0^b} \gamma_{ij}^s \cos(q\omega_{ij} + \phi_{ij}).
\end{aligned} \tag{34}$$

For a point source at the phase center, $q = 0$, $\gamma_{ij}^s = 1$, $\phi_{ij} = 0$ and the SNR of the synthesized image is

$$\begin{aligned} \frac{I_1(0)}{\sqrt{V[i_1(0)]}} &= \frac{ < M > \{I_0^s/(I_0^s + I_0^b)\} \sqrt{n_b}}{\sqrt{(n < M > + P\sigma^2)/2 + < M > (n-2)\{I_0^s/(I_0^s + I_0^b)\}}} \\ &= \frac{ < C > \{I_0^s/(I_0^s + I_0^b)\} \sqrt{(n-1)/n}}{\sqrt{< C > + P\sigma^2 + < C > \{I_0^s/(I_0^s + I_0^b)\} \{2(n-2)/n\}}}. \end{aligned} \quad (35)$$

4. Tradeoff among nC_2 , nC_n and ${}^nC'_n$ Interferometers

We now compare the SNRs of the nC_2 , nC_n and ${}^nC'_n$ interferometers in the case of a point source at the phase center. We are interested in the detection limits of these three interferometers and we consider the situation in which $I_0^s \ll I_0^b$. The total photoelectron count $< C >$ is mostly due to thermal background. In the limit of $I_0^s \ll I_0^b$, the SNR of the nC_2 interferometer, SNR_1 , is given by

$$SNR_1 = \frac{(< C_1 > /2)\{I_0^s/I_0^b\}}{\sqrt{< C_1 > /2 + n_b P_1 \sigma^2 / 2}}, \quad (36)$$

where $< C_1 >$ is the total photoelectron count and P_1 is the total number of pixels per detector. The SNR of the nC_n interferometer, SNR_2 is given by

$$SNR_2 = \frac{ < C_2 > \{I_0^s/I_0^b\} \sqrt{(n-1)/n}}{\sqrt{< C_2 > + P_2 \sigma^2}}, \quad (37)$$

where $< C_2 >$ is the total photoelectron count and P_2 is the total number of detector pixels.

The SNR of the ${}^nC'_n$ interferometer, SNR'_2 is given by

$$SNR'_2 = \frac{ < C'_2 > \{I_0^s/I_0^b\} \sqrt{(n-1)/n}}{\sqrt{< C'_2 > + P'_2 \sigma^2}}, \quad (38)$$

where $< C'_2 >$ is the total photoelectron count and P'_2 is the total number of detector pixels on which superposed fringes are dispersed.

$< C_1 >$, $< C_2 >$, and $< C'_2 >$ depend on the spectral bandwidths, the optical throughputs and detector quantum efficiencies of the interferometers. Here for simplicity we assume that the optical throughputs and detector quantum efficiencies are the same, though in practice the throughputs may differ due to the difference in optical configurations. P_1 , P_2 and P'_2 are determined by the fringe sampling requirements.

Expressions (25) and (35) were derived for spectrally narrow light. In practice this corresponds to the observations of emission lines. For bright objects, it is always advantageous to disperse fringes and reconstruct images at different wavelengths. Especially for emission line objects, spectral dispersion is essential. In this case, (36) and (38) hold for the fringe row corresponding to each spectral bin. For faint objects with broad spectral energy distributions, spectral images formed from individual dispersed fringes need to be coadded to increase detection sensitivities. Below we confirm that (36) and (38) hold also for coadded images of the faint objects.

We first consider the case of the nC_2 interferometer. Let P_x be the number of pixels in the fringe direction and P_y be that in the cross fringe direction. Therefore $P_1 = P_x P_y$. We assume that the photon spectrum within the bandwidth is not steep and the number of photons in one detector row is given by $\langle c_1 \rangle = \langle C_1 \rangle / P_y$. Then the SNR of an image synthesized from a set of fringes in detector rows corresponding to $1/P_y$ of the spectral bandwidth is given by

$$snr_1 = \frac{(\langle c_1 \rangle / 2) \{I_0^s / I_0^b\}}{\sqrt{\langle c_1 \rangle / 2 + n_b P_x \sigma^2 / 2}}. \quad (39)$$

We further assume the total bandwidth is narrow enough so that the source structure does not change within it. In this case, P_y images can be coadded to form a final image. The SNR of the final image is given by

$$\begin{aligned} SNR_1 &= \sqrt{P_y} snr_1 \\ &= \sqrt{P_y} \frac{(\langle c_1 \rangle / 2) \{I_0^s / I_0^b\}}{\sqrt{\langle c_1 \rangle / 2 + n_b P_x \sigma^2 / 2}} \\ &= \frac{(\langle C_1 \rangle / 2) \{I_0^s / I_0^b\}}{\sqrt{\langle C_1 \rangle / 2 + n_b P_x P_y \sigma^2 / 2}} \\ &= \frac{(\langle C_1 \rangle / 2) \{I_0^s / I_0^b\}}{\sqrt{\langle C_1 \rangle / 2 + n_b P_1 \sigma^2 / 2}}. \end{aligned} \quad (40)$$

Therefore (36) holds for spectrally broad light. Similarly one can show that (38) holds for spectrally broad light.

A. Background Limit For Spectrally Narrow Light

For the nC_2 interferometer, the condition for background limited observations is $\langle C_1 \rangle \gg n_b P_1 \sigma^2$. In this case, the SNR is approximated by

$$SNR_1 = \sqrt{\frac{\langle C_1 \rangle}{2}} \frac{I_0^s}{I_0^b}. \quad (41)$$

For the nC_n interferometer, the condition for background limit is $\langle C_2 \rangle \gg P_2 \sigma^2$. In this case, the SNR is approximated by

$$SNR_2 = \sqrt{\langle C_2 \rangle} \frac{I_0^s}{I_0^b} \sqrt{\frac{n-1}{n}}. \quad (42)$$

For spectrally narrow light, the spectral bandwidths do not matter and $\langle C_1 \rangle = \langle C_2 \rangle$. Then

$$SNR_2 = \sqrt{\frac{2(n-1)}{n}} SNR_1, \quad (43)$$

Since $1 < \sqrt{2(n-1)/n} < \sqrt{2}$, for $n > 3$, the nC_n interferometer is preferred in this case. However they differ by at most a factor $\sqrt{2}$ for a large n . There is no difference between the nC_n interferometer and the ${}^nC'_n$ interferometer for spectrally narrow light.

B. Background Limit for Spectrally Broad Light

The fractional bandwidth of the nC_2 interferometer, $\Delta\nu/\nu$ is limited only by the wavelength dependence of the astronomical source structure. Each fringe can be spectrally dispersed on a two dimensional detector to avoid bandwidth smearing. In the general nC_n interferometer with a two dimensional baseline configuration, all the fringes are superposed on a two dimensional detector and they cannot be dispersed. To keep the fringe visibilities high, the fractional bandwidth is limited approximately to D/B where D is the aperture diameter and B is the length of the longest baseline. In the ${}^nC'_n$ interferometer with a one dimensional baseline configuration, dispersed fringes are superposed on a two dimensional detector and the fractional bandwidth, $\Delta\nu/\nu$, is the same as for the nC_2 interferometer. Therefore

$$C_1 = C'_2, \quad (44)$$

where C'_2 is the total number of photoelectron count for the ${}^nC'_n$ interferometer. Since

$$\frac{C_1}{C_2} = \frac{\Delta\nu/\nu}{D/B}, \quad (45)$$

the SNR ratio of the nC_2 and nC_n interferometers is given by

$$\begin{aligned} \frac{SNR_1}{SNR_2} &= \sqrt{\frac{\langle C_1 \rangle}{\langle C_2 \rangle} \frac{n}{2(n-1)}} \\ &= \sqrt{\frac{\Delta\nu}{\nu} \frac{B}{D} \frac{n}{2(n-1)}}. \end{aligned} \quad (46)$$

For a short baseline (small B/D), the nC_n interferometer is superior and for a long baseline, the nC_2 has an advantage. From $SNR_1 = SNR_2$, we obtain $(B/D)_{cross\ over}$ given by

$$\left(\frac{B}{D}\right)_{cross\ over} = \frac{\nu}{\Delta\nu} \frac{2(n-1)}{n}. \quad (47)$$

For a continuum source, the fractional bandwidth $\Delta\nu/\nu$ for which the source structure does not change is the order of 0.1. For $n = 5$, $(B/D)_{cross\ over} = 16$.

From (43), the ratio of SNR for the nC_2 and ${}^nC'_n$ interferometers is given by

$$SNR_1/SNR'_2 = \sqrt{\frac{n}{2(n-1)}}, \quad (48)$$

as in the case of spectrally narrow light. To be fair, we should compare the same one dimensional baseline configuration with different beam combination geometries. In this case, the ${}^nC'_n$ interferometer is superior to the nC_2 interferometer by at most a factor $\sqrt{2}$.

C. Read noise limit

In this subsection, we evaluate the numbers of detector pixels, P_1 , P_2 and P'_2 . There are $2\nu/\Delta\nu$ fringe cycles in each interferogram. For the Nyquist sampling theorem, $4\nu/\Delta\nu$ pixels are needed in the fringe direction. For the nC_2 and ${}^nC'_n$ interferometers, we consider the number of pixels in the cross fringe direction (dispersion direction) in each dispersed fringe. The fractional spectral bandwidth $\Delta\nu^*/\nu$ for which bandwidth smearing is small, is given by $\Delta\nu^*/\nu < D/B$. Therefore for a spectral bandwidth of $\Delta\nu$, we need $\Delta\nu/\Delta\nu^* >$

$(\Delta\nu/\nu)/(D/B)$ pixels in the dispersion direction. Here we take $2(\Delta\nu/\nu)/(D/B)$ pixels as the number of pixels in the cross fringe direction. So the minimum number of pixels of the two dimensional detector is $P_1 = P'_2 = 4\nu/\Delta\nu \times 2(\Delta\nu/\nu)/(D/B) = 8(B/D)$. For the nC_n interferometer, the longest baseline can be aligned to one of the two sides of a two dimensional detector and the minimum number of pixels is $P_2 = (4\nu/\Delta\nu)^2 = 16(B/D)^2$, and the maximum allowed fractional bandwidth is D/B .

In the read noise limit,

$$SNR_1 = \frac{(\langle C_1 \rangle / 2)(I_0^s / I_0^b)}{\sqrt{n_b P_1 \sigma^2 / 2}}, \quad (49)$$

$$SNR_2 = \frac{\langle C_2 \rangle (I_0^s / I_0^b) \sqrt{(n-1)/n}}{\sqrt{P_2 \sigma^2 / 2}}, \quad (50)$$

and

$$SNR'_2 = \frac{\langle C'_2 \rangle (I_0^s / I_0^b) \sqrt{(n-1)/n}}{\sqrt{P'_2 \sigma^2}}, \quad (51)$$

where (44) and (45) hold among $\langle C_1 \rangle$, $\langle C_2 \rangle$, and $\langle C'_2 \rangle$. For a two dimensional baseline configuration, the SNR ratio of the nC_2 and nC_n interferometers is given by

$$SNR_1/SNR_2 = \frac{\sqrt{2}}{n-1} \frac{\Delta\nu}{\nu} \left(\frac{B}{D}\right)^{3/2}. \quad (52)$$

For a short baseline the nC_n interferometer is superior and for a long baseline the nC_2 interferometer is better. From the condition that $SNR_1 = SNR_2$,

$$\left(\frac{B}{D}\right)_{cross\ over} = \left[\frac{(n-1)^2}{2} \left(\frac{\nu}{\Delta\nu}\right)^2 \right]^{\frac{1}{3}}. \quad (53)$$

For $n = 5$, $\Delta\nu/\nu = 0.1$, $(B/D)_{cross\ over} = 9.3$. For a one dimensional baseline configuration, the SNR ratio of the nC_2 and $^nC'_n$ interferometers is given by

$$SNR_1/SNR'_2 = \frac{1}{n-1}. \quad (54)$$

Since $SNR_1 < SNR'_2$ for $n > 3$, the ${}^nC'_n$ interferometer is always superior to the nC_2 interferometer in the read noise limit.

In summary, the nC_n interferometer with a two dimensional baseline configuration has a limited use for a short baseline interferometer or possibly a deployable space interferometer. For a separated spacecraft interferometer with long baselines, the nC_2 is more suitable and the ${}^nC'_n$ interferometer with a one dimensional baseline configuration is even better. In the background limit, the advantage of ${}^nC'_n$ interferometer is small, while in the read noise limit, that is significant. This is simply because of the difference in the number of detectors or that of detector pixels which affect the total read noise.

5. Sensitivity in the Presence of Natural Thermal Background

A. Natural Thermal Background

We are most interested in the potential of an infrared interferometer in the presence of unavoidable natural thermal background. Here we consider the emission from interplanetary dust (IPD) and interstellar dust (ISD) as the natural thermal background.

The brightness of IPD emission depends on ecliptic coordinates.¹¹ Lockman Hole ($\lambda = 137^\circ$, $\beta = 46^\circ$) which is close to the ecliptic pole is the representative of the dark portion of the sky and the ecliptic plane ($\lambda = 122^\circ$, $\beta = 0^\circ$) is that of the bright portion of the sky apart from the galactic plane. IPD emission of the latter is brighter than that of the former by a factor 3 to 4. The spectrum obtained by the Diffuse Infrared Background Experiment (DIRBE) on board the Cosmic Background Explorer (COBE) of the IPD emission we use is given in Ref. 11.

The brightness of ISD emission is correlated with the distribution of the hydrogen column density. The interstellar neutral hydrogen column density of the Lockman Hole is $4-6 \times 10^{23}$ atoms m^{-2} and that of the ecliptic plane is 4.0×10^{24} atoms m^{-2} . To evaluate the dust thermal emission associated with the neutral hydrogen columns, we use the brightness per hydrogen atom at $154 \mu m$ obtained by a rocket-borne telescope, $\nu I_\nu(154)/N(HI) = 3.2 \times 10^{-32} \text{ W sr}^{-1}$, the dust temperature of 16.4 K , and the gray-body dust emissivity law proportional to ν^2 .¹²

In the calculations below, we use the natural thermal background for the Lockman Hole and note here

that the limiting flux is higher by about a factor of 2 for the ecliptic plane when the detection is limited by the natural thermal background.

B. Separated spacecraft interferometer like TPF

For TPF, a four element array with 3.5 m diameter apertures is considered. The telescope apertures are cooled by radiation to 40 K. Here we assume the emissivity of the apertures to be 5%. Varying the length of the longest baseline B , we calculate the SNRs of the nC_2 interferometer for $n = 4$, $D = 3.5$ m, throughput $T = 0.1$, $\sigma = 2e^-$, integration time $t = 100$ seconds, and $\Delta\nu/\nu = 0.1$. The read noise of $\sigma = 2e^-$ may appear small, but such a low level after multiple sampling is set as a goal for NGST.¹³ The coherent integration time, t , is somewhat unknown, but t much longer than 100 seconds is unlikely due to disturbances on the spacecrafts.

In Fig. 4, 5σ detection limits of the nC_2 (solid line) and ${}^nC'_n$ (dashed line) interferometers for 3600 second observations are given for baseline lengths, 100 m and 1 km. Read noise is significant at $\lambda < 5 \mu\text{m}$. In the read noise limit, the detection limits of the nC_2 interferometer with a 100 m baseline and the ${}^nC'_n$ interferometer with a 1 km baseline are almost the same. Around $10 \mu\text{m}$, the detection limits are set by the natural thermal background and at $\lambda > 25 \mu\text{m}$, they are set by the telescope thermal background. For the thermal background limit, the detection limits are baseline independent, because the thermal background is independent of the number of detector pixels. It is noted that there will be no far-infrared capability of TPF itself according to the current concept.

C. Separated spacecraft interferometer like Darwin

For Darwin, a six element array with 1.5 m diameter apertures is considered. Radiation cooling is expected to cool the telescope apertures to 30 K. Here we again assume the emissivity of the apertures to be 5%. We calculate the SNRs of the nC_2 and ${}^nC'_n$ interferometers for $n = 6$, $D = 1.5$ m, $T = 0.1$, $\sigma = 2e^-$, integration time $t = 100$ seconds, and $\Delta\nu/\nu = 0.1$. In Fig. 5, 5σ detection limits for 3600 second observations are given as functions of wavelength for baseline lengths, 100 m, and 1 km. For 1 km baseline, the effect of read noise is visible up to $10 \mu\text{m}$. With the number of apertures, $n = 6$, the ${}^nC'_n$ interferometer with 1 km baseline is more sensitive than the nC_2 interferometer with 100 m baseline in the read noise limit.

D. Single spacecraft interferometer

Here we consider a deployable interferometer with five 1.5 m apertures and the two dimensional nC_n beam combination geometry. We assume actively cooled telescope apertures of 5 K and emissivity of 5%. The system throughput T is assumed to be 0.1. We also assume $\sigma = 2e^-$, integration time $t = 100$ seconds, and $\Delta\nu/\nu = D/B$. We consider the baseline lengths of 10, 30, and 100 m. In Fig. 6, 5 σ detection limits for 3600 second observations are given as functions of wavelength. The baseline length of 100 m may be too large for the nC_n geometry due to the narrow fractional bandwidth and the effect of read noise. The two dimensional nC_n interferometer has an advantage for a compact array as discussed above.

6. Capability for a deep far-infrared survey and comparison with observatories

In this section, we investigate the potential of a TPF-like space interferometer for a deep far-infrared survey which is important in studying the galaxy formation history.

We first summarize the current status of the subject. In Fig. 7, source confusion limits at 90 and 170 μm of different observatories in space predicted by the model E of Guiderdoni et al.¹⁴ are compared with those estimated from the recent Infrared Space Observatory (ISO) observations^{15, 16}. The model E of Guiderdoni et al. is known as one of the very successful models which can explain the Infrared Astronomical Satellite (IRAS) 60 μm counts, ISO 15 μm counts, and cosmic far-infrared background radiation recently detected by the Far Infrared Absolute Spectrophotometer (FIRAS) on board COBE.

At 90 μm , the true confusion limit is one order of magnitude greater than the limit estimated by the model at an angular resolution of 10'' or for a telescope diameter of 2.2 m. The model predictions of the confusion limits of SPICA or FIRST at both 90 and 170 μm should be regarded as lower limits.

In Fig. 8, 5 σ detection limits of a TPF-like nC_2 interferometer (4 x 3.5 m) for telescope temperatures, 5, 10, 20, and 40 K with 5% emissivity are compared with those of NGST, SPICA, and FIRST (Nakagawa et al. 1998). The assumed total observing time is 3600 seconds. As for the interferometer, we assume $T = 0.1$, $\sigma = 2e^-$, $\Delta\nu/\nu = 0.1$, coherent integration time $t = 100$ seconds, and $B = 100$ m. In Fig. 9, 5 σ detection limits of a TPF-like ${}^nC'_n$ interferometer are calculated for the same conditions.

Before interpreting Figs. 8 and 9, the limitations of the comparison between the SNRs of an interferom-

eter and a single telescope must be noted. For the SNR of the interferometer, we use that for a point source. In reality there may be multiple sources and some of them may be resolved, in which case the complex visibility $\gamma \exp(i\phi)$ must be obtained by (4) and be inserted into the SNR formula. The sensitivity of the observatory is also given for a point source. However a single telescope can observe multiple point sources at once, while the interferometer needs to cover sufficient uv points or baseline configurations to recover multiple sources. So necessary observing time is likely to be greater for the interferometer. We proceed with the comparison with this limitation in mind.

In the near infrared, the ${}^nC'_n$ interferometer is more sensitive than the nC_2 interferometer. However the spatial resolution of NGST is sufficient and its sensitivity is superior to both interferometers for the purpose of galaxy count. In the mid infrared, the sensitivities of the interferometers are comparable to the sensitivity of SPICA though spatial resolutions are different.

The advantage of the interferometers is obvious in the far infrared. In the present concept of TPF, a telescope temperature of 40 K is assumed. Even with 40 K telescopes, the interferometers are more sensitive than SPICA or FIRST at $\lambda > 100 \mu\text{m}$. It is clear from the the result of calculation for 5 K telescopes that an actively cooled interferometer in the far infrared regardless of the beam combination geometry is ideal for detecting faint galaxies which are otherwise undetected due to source confusion. Bright starburst galaxies will be detectable at $170 \mu\text{m}$ out to $z = 4$ with the actively cooled interferometer. The survey may not only identify far-infrared luminous galaxies at high redshift as IRAS did at low redshift, but may even detect a galaxy population which is undetectable by NGST in the near infrared due to the weakness of stellar emission extinguished by dust.

7. Conclusions

In this paper, we have studied the sensitivities of space borne infrared interferometers for the purpose of general synthesis imaging. Our primary conclusions follow.

- (1) We have derived the expressions for the SNRs of nC_2 and nC_n interferometers in the presence of source shot noise, thermal background shot noise, and detector read noise.
- (2) We have investigated the tradeoff between the nC_2 and nC_n interferometers for a two dimensional baseline configuration and found that the nC_2 geometry is suitable for a long baseline interferometer, while

the nC_n geometry is fitted to a short baseline deployable interferometer. For a one dimensional baseline configuration, we have found that the ${}^nC'_n$ interferometer is superior especially in the case of read noise limited observations.

(3) We have presented the detection limits of separated spacecraft interferometers like TPF and Darwin in the presence of the natural thermal background as functions of wavelength. The comparison of a TPF-like interferometer with NGST, SPICA and FIRST has revealed that at $\lambda > 100 \mu\text{m}$, an interferometer is more sensitive than SPICA or FIRST. This is true with only radiation cooling of the apertures.

We thank David Saint-Jacques and the anonymous referee for comments on the manuscript. TN is supported by Grant-in-Aid for Scientific Research of the Japanese Ministry of Education, Culture, Sports, and Science (No. 10640239).

A Variance $V[i_2(q)]$

The derivation of the variance $V[i_2(q)]$ is analogous to that of $V[i_1(q)]$ but more complicated. We utilize the results by PK89 whenever possible.

$$\begin{aligned}
V[i_2(q)] &= \langle i_2(q)^2 \rangle - \langle i_2(q) \rangle^2 \\
&= \sum_{i < j} \sum_{k < l} [\langle Re(y_{ij})Re(y_{kl}) \rangle - \langle Re(y_{ij}) \rangle \langle Re(y_{kl}) \rangle] \cos(\omega_{ij}q) \cos(\omega_{kl}q) \\
&\quad - [\langle Re(y_{ij})Im(y_{kl}) \rangle - \langle Re(y_{ij}) \rangle \langle Im(y_{kl}) \rangle] \cos(\omega_{ij}q) \sin(\omega_{kl}q) \\
&\quad - [\langle Im(y_{ij})Re(y_{kl}) \rangle - \langle Im(y_{ij}) \rangle \langle Re(y_{kl}) \rangle] \sin(\omega_{ij}q) \cos(\omega_{kl}q) \\
&\quad + [\langle Im(y_{ij})Im(y_{kl}) \rangle - \langle Im(y_{ij}) \rangle \langle Im(y_{kl}) \rangle] \sin(\omega_{ij}q) \sin(\omega_{kl}q) \tag{55}
\end{aligned}$$

As in §2, the problem of estimating the variance in the image thus reduces to that of estimating three types of covariance term: $\text{cov}[Re(y_{ij}), Re(y_{kl})]$, $\text{cov}[Re(y_{ij}), Im(y_{kl})]$, $\text{cov}[Im(y_{ij}), Im(y_{kl})]$. Using (20), we obtain the covariance of the real components of a pair of fringe phasors as

$$\begin{aligned}
\text{cov}[Re(y_{ij}), Re(y_{kl})] &= \sum_p (\langle k(p) \rangle + \sigma^2) \cos(p\omega_{ij}) \cos(p\omega_{kl}) \\
&= \sum_p \left[\langle Q_0 \rangle n + \sigma^2 + \langle Q_0 \rangle \sum_{g < h} \gamma_{gh} \cos(p\omega_{gh} + \phi_{gh}) \right]
\end{aligned}$$

$$\times \cos(p\omega_{ij}) \cos(p\omega_{kl}) \quad (56)$$

Every cosine can be written as the sum of exponential functions:

$$\begin{aligned} \sum_p \cos(p\omega_{ij}) \cos(p\omega_{kl}) &= \sum_p \frac{\exp(ip\omega_{ij}) + \exp(-ip\omega_{ij})}{2} \frac{\exp(ip\omega_{kl}) + \exp(-ip\omega_{kl})}{2} \\ &= \sum_p \left[\frac{\exp(ip(\omega_{ij} + \omega_{kl}))}{4} + \frac{\exp(ip(\omega_{ij} - \omega_{kl}))}{4} \right. \\ &\quad \left. + \frac{\exp(-ip(\omega_{ij} + \omega_{kl}))}{4} + \frac{\exp(-ip(\omega_{ij} - \omega_{kl}))}{4} \right] \\ &= P \frac{\delta_{ik}\delta_{jl}}{2}. \end{aligned} \quad (57)$$

In (57), from nonredundancy of baselines, $\pm\omega_{ij} \pm \omega_{kl} \neq 0$ for $i \neq k, j \neq l$. Similarly to the two frequency case, the three frequency case can be computed.

Following PK89, we now impose an additional condition to ordinary nonredundancy in order to simplify the calculations. This condition, hereafter referred to as the nonredundancy of triangles, concerns three-frequency combinations. Specifically, we assume that

$$\omega_{gh} \pm \omega_{ij} \pm \omega_{kl} \neq 0, \quad (58)$$

unless (gh), (ij), and (kl) form the sides of a triangle. This condition is easily fulfilled for a space interferometer with a small number of apertures. With the nonredundancy of triangles for $i < j$ and $k < l$,

$$\sum_p \sum_{g < h} \gamma_{gh} \cos(p\omega_{gh} + \phi_{gh}) \cos(p\omega_{ij}) \cos(p\omega_{kl}) = \frac{\gamma \cos \phi}{2} \Delta_{ij,kl} \quad (59)$$

where the symbol $\Delta_{ij,kl}$ unless ij and kl baselines form two sides of a triangle, in which case it equals 1, and $\gamma \exp(i\phi)$ is the phasor on the third side of that triangle.

From Eqs (57) and (59),

$$\text{cov}[Re(y_{ij}), Re(y_{kl})] = \frac{< M > n + P\sigma^2}{2} \delta_{ik}\delta_{jl} + < M > \frac{\gamma \cos \phi}{2} \Delta_{ij,kl}. \quad (60)$$

Similarly,

$$\text{cov}[Im(y_{ij}), Im(y_{kl})] = \frac{< M > n + P\sigma^2}{2} \delta_{ik} \delta_{jl} \mp < M > \frac{\gamma \cos \phi}{2} \Delta_{ij,kl}. \quad (61)$$

Everywhere in this section, the upper sign (or expression) is the correct one when the sides (ij) and (kl) of the triangle meet at that vertex for which the label has a value intermediate to those of the two vertices, i.e., either when $i < j = k < l$ or $k < l = i < j$. The lower sign (or expression) is the correct one otherwise, i.e., when $i = k$ or when $j = l$.

Evaluation of $\text{cov}[Re(y_{ij}), Im(y_{kl})]$ is identical with that for the case with Poisson noise alone as obtained in PK89:

$$\text{cov}[Re(y_{ij}), Im(y_{kl})] = < M > \frac{\gamma \sin \phi}{2} \Delta_{ij,kl} \times \left\{ \begin{array}{c} +1 \\ \text{sgn}(i - j) \text{ for } i = k, \text{sgn}(i - k) \text{ for } j = l \end{array} \right\}, \quad (62)$$

where $\text{sgn}(x)$ is $+1$ if $x > 0$ and -1 if $x < 0$.

Furthermore,

$$\text{cov}[Re(y_{ij}), Im(y_{kl})] = \pm \text{cov}[Im(y_{ij}), Re(y_{kl})]. \quad (63)$$

Now we evaluate the variance,

$$\begin{aligned} V[i_2(q)] &= \frac{n < M > + P\sigma^2}{2} \sum_{i < j} [\cos^2(q\omega_{ij}) + \sin^2(q\omega_{ij})] \\ &+ \frac{< M >}{2} \left\{ \sum_{i < j} \sum_{k < l} \Delta_{ij,kl} \cos[q(\omega_{ij} \pm \omega_{kl})] \gamma \cos \phi \right. \\ &\quad - \sum_{i < j = k < l} \sin[q(\omega_{ij} + \omega_{kl})] \gamma_{il} \sin \phi_{il} \\ &\quad - \sum_{k < l = i < j} \sin[q(\omega_{ij} + \omega_{kl})] \gamma_{kj} \sin \phi_{kj} \\ &\quad - \sum_{j < l} (n - l + j - 1) \sin[q(\omega_{il} + \omega_{ij})] \gamma_{jl} \sin \phi_{jl} \\ &\quad \left. - \sum_{l < j} (n - j + l - 1) \sin[q(-\omega_{il} + \omega_{ij})] \gamma_{lj} \sin \phi_{lj} \right\}. \end{aligned} \quad (64)$$

By relabeling the indices slightly and combining the various sums using simple trigonometric identities, we obtain the final expression of $V[i_2(q)]$, (34).

B Remapping of Pupils

The anonymous referee pointed out the possibility of pupil remapping which changes the interpretation of the interferometer types. We do not consider this possibility in the main text, but mention here the view based on it.

The distinction between the nC_2 , nC_n , and ${}^nC'_2$ refers actually to the “output pupil” (arrangement of the beams immediately before fringe detection) rather than to the configuration of the interferometer as a whole. One could use a two dimensionally distributed array with a linear nonredundant arrangement of the beams before the detector like the one shown in Fig. 3, with a remapping stage during data processing. Any two dimensional interferometer can therefore accommodate spectral dispersion in principle.

However such a scheme would require additional optics, affecting the system throughput and thermal environment. It also makes the image reconstruction procedure complex. We therefore would not include this scheme in this comparative analysis.

References

1. H. Murakami, "Japanese infrared survey mission IRIS (ASTRO-F)", in *Space Telescope and Instruments*, SPIE, **3356**, p471-477, (1998)
2. J. L. Fanson, G. G. Fazio, J. R. Houck, T. Kelley, G. H. Rieke, D. J. Tenerelli, & M. Whitten, "Space Infrared Telescope Facility" in *Space Telescope and Instruments*, V. P. Y. Bely & J. B. Breckinridge, eds., SPIE, **3356**, p478-491 (1998)
3. G. Pilbratt, in "The Far InfraRed and Submillimeter Universe", Wilson, A. ed., ESA EP-401, p7 (1997)
4. T. Nakagawa, M. Hayashi, M. Kawada, H. Matsuhara, T. Matsumoto, H. Murakami, H. Okuda, T. Onaka, H. Shibai, & M. Ueno, "HII/L2 mission: future Japanese infrared astronomical mission" in *Space Telescope and Instruments*, SPIE, **3356**, p462-470 (1998)
5. The TPF Science Working Group, C. A. Beichman, N. J. Woolf, & C. A. Lindensmith eds., *TPF: Terrestrial Planet Finder, Origins of Stars, Planets and Life*, JPL Publication 99-003 (1999)
6. A. J. Penny, A. Leger, J.-M. Mariotti, C. Schalinski, C. L. Eiroa, J. Robin, & M. Fridlund, "DARWIN interferometer" in *Astronomical Interferometry*, R. D. Reasenberg ed., SPIE, **3350**, p666-671 (1998)
7. S. Prasad & S. R. Kulkarni, "Noise in optical synthesis images. I. Ideal Michelson interferometer", *J. Opt. Soc. Am. A* **6**, 1702-1714 (1989)
8. R. A. Perley, F. R. Schwab, & A. H. Bridle, *Synthesis Imaging in Radio Astronomy*, NRAO Workshop No. 21, ASP Conference Series, San Francisco (1989)
9. J. F. Walkup & J. W. Goodman, "Limitations of fringe parameter estimation at low light levels", *J. Opt. Soc. Am.*, **63**, 399-409 (1973)

10. J. W. Goodman, *Statistical Optics*, Wiley, NY (1985)

11. T. Kelsall, “The COBE Diffuse Infrared Background Experiment Search for Cosmic Infrared Background. II. Model of the Interplanetary Dust Cloud”, 1998, *Astrophys. J.*, **508**, 44-73 (1998)

12. M. Kawada, J. J. Bock, V. V. Hristov, A. E. Lange, H. Matsuura, T. Matsumoto, S. Matsuura, P. D. Mauskopf, P. L. Richards, & M. Tanaka, “A rocket-borne observation of the far-infrared sky at high Galactic latitude”, *Astrophys. J.*, **425**, L89-L92 (1994)

13. The NGST study team, H. S. Stockman ed., “The Next Generation Space Telescope, Visiting a Time When Galaxies were Young”, (AURA Inc.) (1997)

14. B. Guiderdoni, E. Hivon, F. R. Bouchet, & B. Maffei, “Semi-analytic modelling of galaxy evolution in the IR/submm range”, *Mon. Not. Royal Astron. Soc.*, **295**, 877-898 (1998)

15. J. L. Puget, G. Lagache, D. L. Clements, W. T. Reach, H. Aussel, F. R. Bouchet, C. Cesarsky, F. X. Desert, H. Dole, D. Elbaz, A. Franceschini, B. Guiderdoni, & A. F. M. Moorwood, “FIRBACK. I. A deep survey at 175 microns with ISO, preliminary results”, *Astron. Astrophys.* **345**, 29-35 (1999)

16. H. Matsuura, K. Kawara, Y. Sato, Y. Taniguchi, H. Okuda, T. Matsumoto, Y. Sofue, K. Wakamatsu, L. L. Cowie, R. D. Joseph, & D. B. Sanders, “ISO deep far-infrared survey in the Lockman Hole. II. Power spectrum analysis: evidence of a strong evolution in number counts”, *Astron. Astrophys.* **361**, 407-414 (2000)

Fig. 1. Focal plane interferometer and a detector array. This configuration exists for each baseline of an nC_2 interferometer. The effect of shot noise on photodetection process has been fully formulated for this situation. For spectrally broad light, the fringe can be dispersed in the cross fringe direction if a two-dimensional detector is used.

Fig. 2. Two-dimensional 3C_3 interferometer. Fringes are superposed at the focal plane of a two dimensional detector. Since the fringes cannot be dispersed, the spectral bandwidth of this interferometer is limited.

Fig. 3. One-dimensional ${}^3C'_3$ interferometer. One dimensional fringes are dispersed in the cross fringe direction and superposed at the focal plane of a two dimensional detector. Spectrally broad light can be observed by an nC_n interferometer with one dimensional baselines.

Fig. 4. Detection limits of a TPF-like interferometer. 5σ detection limits are plotted as functions of wavelength for the maximum baseline lengths given in the figure for an nC_2 interferometer (solid) and a one-dimensional ${}^nC'_n$ interferometer (dash). Assumptions about other parameters are given in the text.

Fig. 5. Detection limits of a Darwin-like interferometer. 5σ detection limits are plotted as functions of wavelength for the maximum baseline lengths given in the figure for an nC_2 interferometer (solid) and a one-dimensional ${}^nC'_n$ interferometer (dash). Assumptions about other parameters are given in the text.

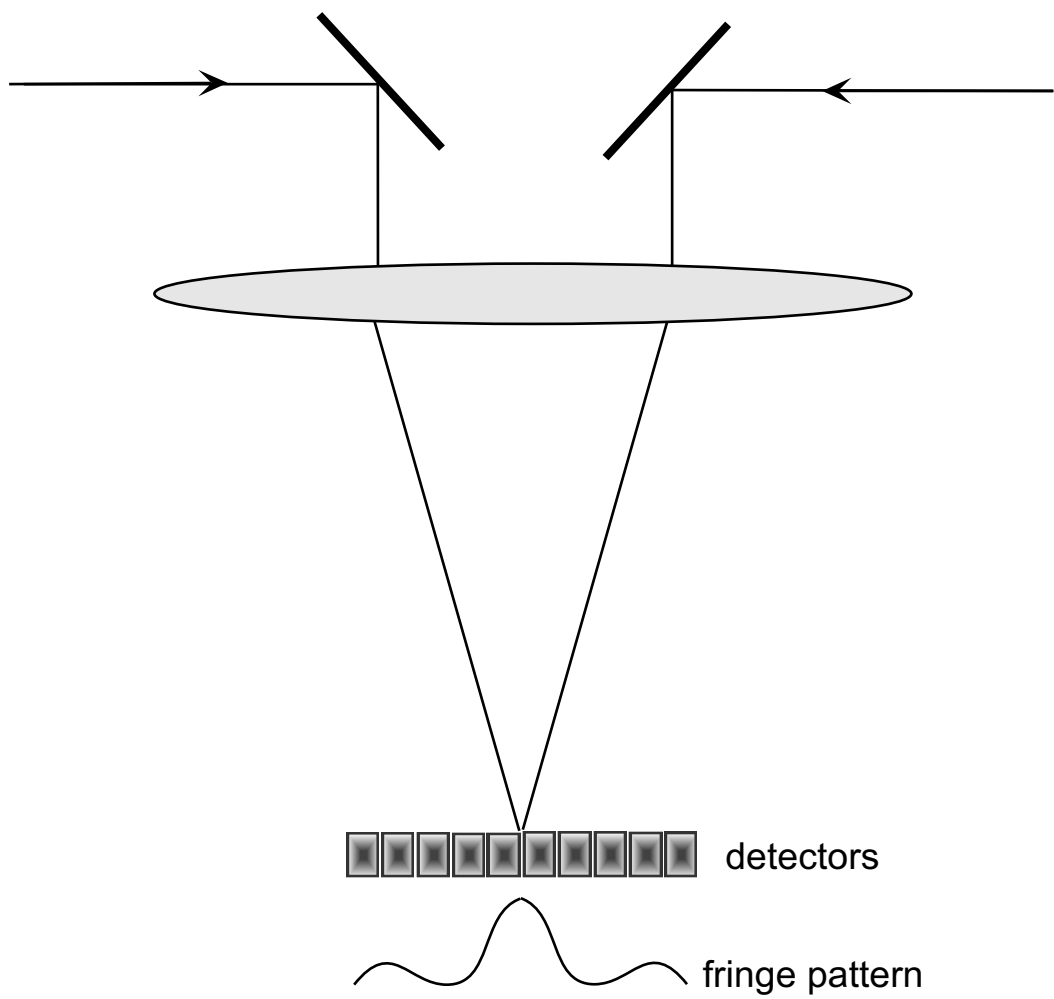
Fig. 6. Detection limits of a five element compact array with artificially cooled apertures. 5σ detection limits of a two-dimensional nC_n interferometer are plotted as functions of wavelength for the maximum baseline lengths given in the figure. Assumptions about other parameters are given in the text.

Fig. 7. Confusion limits of monolithic observatories. The confusion limits predicted from the model E of Guiderdoni et al.¹⁴ (solid line) are compared with those estimated from ISO observations by Matsuura et al.¹⁶ (polygon) and Puget et al.¹⁵ (triangle).

Fig. 8. Comparison with monolithic observatories. The sensitivity of an nC_2 interferometer composed of four 3.5 m apertures is plotted for telescope temperatures of 5, 10, 20, and 40 K with emissivity of 5%. The

maximum baseline length is assumed to be 100 m. Dashed lines denote the sensitivities of NGST, SPICA, and FIRST given for comparison.

Fig. 9. Comparison with monolithic observatories. The sensitivity of a one dimensional ${}^nC'_n$ interferometer composed of four 3.5 m apertures is plotted for telescope temperatures of 5, 10, 20, and 40 K with an emissivity of 5%. The maximum baseline length is assumed to be 100 m. Dashed lines denote the sensitivities of NGST, SPICA, and FIRST given for comparison.



This figure "Figure2.gif" is available in "gif" format from:

<http://arxiv.org/ps/astro-ph/0011309v1>

This figure "Figure3.gif" is available in "gif" format from:

<http://arxiv.org/ps/astro-ph/0011309v1>

